



ELSEVIER

Contents lists available at ScienceDirect

Acta Biomaterialia

journal homepage: www.elsevier.com/locate/actbio

Full length article

Analysis of the bone ultrastructure around biodegradable Mg–xGd implants using small angle X-ray scattering and X-ray diffraction

Berit Zeller-Plumhoff^{a,*}, Carina Malich^a, Diana Krüger^a, Graeme Campbell^a, Björn Wiese^a, Silvia Galli^b, Ann Wennerberg^c, Regine Willumeit-Römer^{a,*}, D.C. Florian Wieland^a

^a Division of Metallic Biomaterials, Helmholtz Zentrum Geesthacht, Institute for Materials Research, Max-Planck-Straße 1, 21502 Geesthacht, Germany

^b Department of Prosthodontics, University of Malmö, Faculty of Odontology, Carl Gustafs väg 34, Klerken, 20506 Malmö, Sweden

^c Department of Odontology, University of Gothenburg, Medicinargatan 12 f, 41390 Göteborg, Sweden

ARTICLE INFO

Article history:

Received 26 July 2019

Revised 11 November 2019

Accepted 12 November 2019

Available online xxx

Keywords:

Biodegradable magnesium implants

Bone ultrastructure

Bone-implant interface

ABSTRACT

Magnesium alloys are increasingly researched as temporary biodegradable metal implants in bone applications due to their mechanical properties which are more similar to bone than conventional implant metals and the fact that Magnesium occurs naturally within the body. However, the degradation processes in vivo and in particular the interaction of the bone with the degrading material need to be further investigated. In this study we are presenting the first quantitative comparison of the bone ultrastructure formed at the interface of biodegradable Mg–5Gd and Mg–10Gd implants and titanium and PEEK implants after 4, 8 and 12 weeks healing time using two-dimensional small angle X-ray scattering and X-ray diffraction. Differences in mineralization, orientation and thickness of the hydroxyapatite are assessed. We find statistically significant ($p < 0.05$) differences for the lattice spacing of the (310)-reflex of hydroxyapatite between titanium and Mg–xGd materials, as well as for the (310) crystal size between titanium and Mg–5Gd, indicating a possible deposition of Mg within the bone matrix. The (310) lattice spacing and crystallite size further differ significantly between implant degradation layer and surrounding bone ($p < 0.001$ for Mg–10Gd), suggesting apatite formation with significant amounts of Gd and Mg within the degradation layer.

Statement of significance

Biodegradable Magnesium-based alloys are emerging as a viable alternative for temporary bone implant applications. However, in order to understand if the degradation of the implant material influences the bone ultrastructure, it is necessary to study the bone structure using high-resolution techniques. We have therefore employed 2D small angle X-ray scattering and X-ray diffraction to study the bone ultrastructure surrounding Magnesium–Gadolinium alloys as well as Titanium and PEEK alloys at three different healing times. This is the first time, that the bone ultrastructure around these materials is directly compared and that a statistical evaluation is performed. We found differences indicating a possible deposition of Mg within the bone matrix as well as a local deposition of Mg and/or Gd at the implant site.

Data availability statement

The raw/processed data required to reproduce these findings cannot be shared at this time as the data also forms part of an ongoing study.

© 2019 Published by Elsevier Ltd on behalf of Acta Materialia Inc.

Abbreviations: SAXS, small angle X-ray scattering; XRD, X-ray diffraction; HAP, hydroxyapatite; Mg, magnesium, Gd, gadolinium.

* Corresponding authors.

E-mail addresses: berit.zeller-plumhoff@hzg.de (B. Zeller-Plumhoff), regine.willumeit@hzg.de (R. Willumeit-Römer).

<https://doi.org/10.1016/j.actbio.2019.11.030>

1742-7061/© 2019 Published by Elsevier Ltd on behalf of Acta Materialia Inc.

Please cite this article as: B. Zeller-Plumhoff, C. Malich and D. Krüger et al., Analysis of the bone ultrastructure around biodegradable Mg–xGd implants using small angle X-ray scattering and X-ray diffraction, Acta Biomaterialia, <https://doi.org/10.1016/j.actbio.2019.11.030>

1. Introduction

Biodegradable implants are emerging as a viable alternative to the widely used titanium implants in cases where the implant is not intended for permanent use in the body and thus requires a second surgical intervention for removal. In the case of biodegradable bone implants, the implant is degrading within the body, whilst new bone tissue is formed around it. Magnesium (Mg) in particular is a promising candidate for biodegradable metal implants due to its mechanical properties which are more similar to bone than conventional implant metals and the fact that Mg occurs naturally within the body [1]. The degradation rate of magnesium alloys can be tailored, depending for example on the choice of alloying elements, the material microstructure, surface geometries and treatments [2–4].

Many studies have looked at the in vitro degradation of different Mg alloys, with and without cells [4–9], some have also taken the in vivo degradation into account [4,8,9]. The degradation layer of Mg and its alloys in vivo and in vitro in cell media contains both Calcium and Phosphate, which indicates apatite formation [6,9]. However, up to date few studies have looked at the bone formation around the biodegradable implant, both on a microscopic and ultrastructural level. Bone is a hierarchical material, whose ultrastructural building blocks are fibrils, which make up the osteon lamellae [10]. The fibrils have a composite structure formed by type I collagen and hydroxyapatite crystal platelets (HAP) [10–12]. The platelets measure around $3 \times 25 \times 50$ nm [11,13,14], but vary with certain conditions such as age [15]. The HAP crystal is of hexagonal lattice structure with $a = b = 9.4$ Å and $c = 6.8$ Å [16]. Within the bone, the HAP c-axis aligns parallel to the long axis the collagen fibers [17,18]. The bone ultrastructure can be studied with various techniques [19], namely small angle X-ray scattering (SAXS) and X-ray diffraction (XRD), which reveal platelet orientation and thickness and crystal size and lattice spacing for particular crystal reflexes, respectively [19]. These are the parameters that determine the bone quality and the mechanical properties of the bone matrix. In osteogenesis imperfecta where bone strength is impaired it has for example been shown that HAP platelets are distinctly smaller and of different composition [20].

Grünewald et al. in particular have used high-resolution SAXS and XRD and micro X-ray fluorescence (μ XRF) to investigate the ultrastructure and chemical make-up of the bone surrounding Mg alloys ZX50 and WZ21, suggesting the coinciding of Mg accumulation around blood vessels and osteocyte lacunae with HAP lattice contractions [21]. Using lower resolution SAXS Grünewald et al. have further shown a temporary decrease in platelet thickness in the newly forming bone around WZ21 alloy, which normalizes with increasing healing time [22]. However, the studies presented by Grünewald et al. lacked comparison to widely used implant materials, such as titanium and polyether ether ketone (PEEK) and consisted of a qualitative rather than quantitative comparison. The ultrastructure of bone surrounding titanium implants was investigated by Hoerth et al. [23] and Büniger et al. [24], however, due to the permanent nature of the implants, the time-dependency of the bone ultrastructure was not taken into account.

In this study we are presenting the first quantitative comparison of the ultrastructure development of bone surrounding non-degradable implant materials already used in the clinic (titanium, PEEK) and biodegradable implants made from Magnesium-Gadolinium alloys (Mg-xGd, where x denotes the Gd weight percentage) for healing times of 4, 8 and 12 weeks. The Mg-xGd alloys were chosen in particular, as Gd enhances the mechanical properties of Mg [3] and results in slower degradation rates in vitro until a weight percentage of 10 is reached [3,8,9]. Mg-10Gd implants have further been found to result in relatively high bone-to-implant contact, thus indicating good osseointegration [25].

2. Materials and methods

2.1. Material processing

Slotted grub screws were manufactured from extruded Magnesium alloys with two different weight percentages (wt%) of Gadolinium, i.e., 5 wt% and 10 wt%, denoted Mg-5Gd and Mg-10Gd, as previously published [26]. The screws were 4 mm long, 2 mm in diameter, and had an M2 thread. PEEK and Titanium screws purchased from Promimic AB (Mölnådal, Sweden) were used as reference materials.

2.2. Animal experiments

The animal experiment was conducted after ethical approval by the ethical committee at the Malmö/Lund regional board for animal research, Swedish Board of Agriculture, with the approval number DNR M 188-15. 30 Sprague Dawley adult male rats were used for this study. The animals were anesthetized with an intraperitoneal dose of Fentanyl 300 μ g/kg + Dexmedetomidin 150 μ g/kg and then the legs were shaved and disinfected with chlorhexidine ethanol solution 0.5 mg/ml (Klorhexidinsprit; Fresenius Kabi, Uppsala Sweden). The area of the tibiae was infiltrated with 1 ml of local anaesthetic and then a full thickness flap was elevated to expose the tibia metaphysis. An osteotomy was created in the area of the tibial metaphysis of each tibia with a round drill of 1.4 mm diameter and then enlarged with a cylindrical bur of 1.6 mm diameter, under constant irrigation with sterile saline. Thereafter, the osteotomies were tapped and screws were implanted with a manual screwdriver. Each rat received 2 screws, one in the left and one in the right tibia. The rats received either two Mg-based screws (one Mg-10Gd and one Mg-5Gd) or two non-Mg screws (PEEK and Ti), and the allocation was random. The flap was then sutured with a resorbable Vycril 4.0 suture in the muscular layer and a silk suture in the skin. An analgesic dose of Buprenorfin of 0.01–0.05 mg/kg (Temgesic, Indivior Europe Limited, Dublin, Ireland) was given. The rats were housed in cages in groups of 2 or 3 animals each. They were fed ad libitum and anti-inflammatory medications were administered the day after the surgery. Overall, 18 rats were implanted per material group and time point, i.e. 108 animals overall.

2.3. Sample processing for imaging

After 4, 8 or 12 weeks of healing the rats were euthanized by a lethal dose of anaesthetic. After the rats were sacrificed, the legs were dissected to extract the tibia and then cylindrical or box-shaped explants with a diameter/width of 5 mm were cut from the rat's femur with rotating burs under irrigation. The samples were dehydrated in increasing concentration of ethanol and then they were critical point dried for high-resolution computed tomography experiments. The bone-implants blocks were subsequently rehydrated and embedded in methylmetacrylate by LLS Rowiak LaserLabSolutions GmbH (Hanover, Germany). For the present experiment, explants originating from 30 rats were randomly chosen. Namely, 9 rats sacrificed at 4 weeks, with 3 Mg-10Gd, 3 Mg-5Gd, 3 Ti and 0 PEEK; 10 rats sacrificed at 8 weeks, 2 Mg-10Gd, 3 Mg-5Gd, 3 PEEK, 2 Ti; and 11 rats sacrificed at 12 weeks, 3 Mg-10Gd, 3 Mg-5Gd, 3 PEEK, 2 Ti. The embedded explants were cut into halves along the implant long axis using a 0.2 mm diamond band saw (Exakt Saw 300 CL, Exakt Technologies, Inc. OK, USA). Subsequently, one half was processed by LLS Rowiak for X-ray scattering experiments by laser cutting. Three to five thin sections of 10 μ m thickness were cut using laser cutting and mounted on kapton tape.

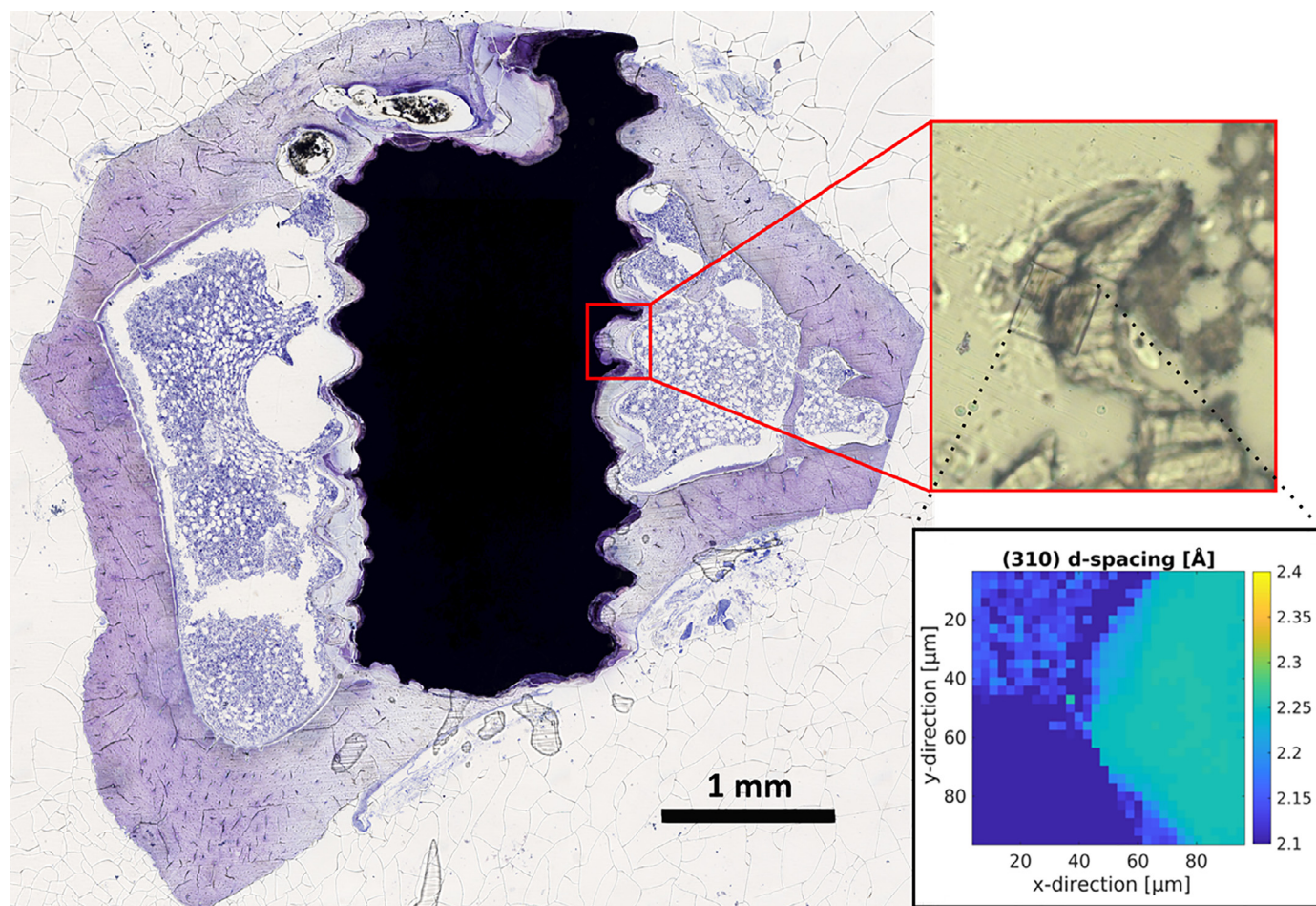


Fig. 1. Exemplary histological thin section of a Mg-5Gd implant after 12 weeks of healing time stained with toluidine blue. The red-boxed subfigure shows a zoom into the scanned region of $90\ \mu\text{m} \times 90\ \mu\text{m}$ in the corresponding thin section of the sample mounted on kapton tape. The rectangular scanned region is clearly discernible due to the damage the focused X-ray beam causes within the kapton tape. An exemplary map of the computed (310) lattice spacing for this region is displayed within the black box. A difference in lattice spacing between the degradation layer of the screw (upper left corner) and the bone (right hand side) is visible. (For interpretation of the references to color in this figure legend, the reader is referred to the web version of this article.)

2.4. Small angle X-ray scattering and X-ray diffraction experiments

Experiments were performed in two separate beam times at the P03 nano-focus end station [27,28] at the PETRA III storage ring, Deutsches Elektronen-Synchrotron (DESY). The X-ray energy was set to 12.8 keV and 13.7 keV, respectively. A Pilatus 1 M detector (DECTRIS Ltd., Baden-Daettwil, Switzerland) at a distance of approximately 2.24 m behind a flight tube was used to obtain the SAXS signal and a LAMBDA 750k detector (X-Spectrum GmbH, Hamburg, Germany) was placed at an angle next to the flight tube at a distance of approximately 18–19 cm to the focal point to record the XRD signal. Calibration of the XRD detector was performed using lanthanum hexaboride, whilst the SAXS detector was calibrated using silver behenate. Regions of $90\ \mu\text{m} \times 90\ \mu\text{m}$ were scanned with a step size of $2.88\ \mu\text{m}$. Exposure times were set to 5 (at 13.7 keV) and 10 (at 12.8 keV) seconds, respectively. Using a custom-build frame, 7 samples on kapton tape were mounted simultaneously. Fig. 1 displays an exemplary histological thin section of a Mg-5Gd implant after 12 weeks of healing time. The red-boxed subfigure shows a zoom into the scanned region in the corresponding thin section of the sample mounted on kapton tape. As the laser cannot penetrate the metal, only degradation layer and bone are cut and transferred onto the kapton tape. The rectangular scanned region is clearly discernible using light microscopy due to the damage the focused X-ray beam causes

Table 1

Number of regions at implant interface scanned per material and healing time.

Implant material	Healing time			Total
	4 weeks	8 weeks	12 weeks	
Mg-10Gd	4	4	6	14
Mg-5Gd	4	4	4	12
PEEK	–	6	3	9
Titanium	7	9	6	22
Total number of scanned interface regions:				57

within the kapton tape. An exemplary map of the computed (310) lattice spacing for this region is displayed within the black box. It can be excluded that the radiation damage had any influence on the results as multiple exposures at one spot on the samples did not show any change in the scattering pattern. Furthermore, using microscopy it can be shown that bone structure and the damaged areas are situated in different focal planes.

Table 1 shows the number of regions from the bone-implant interface that were imaged per material and time point, with 57 regions being scanned overall. The regions to be scanned were identified using an in-line microscope. They were selected to contain the bone-implant interface, which could be identified based on the thread morphology of the in-grown bone (see red box Fig. 1), but placed randomly within the whole of the interfacial region. Ad-

ditionally, one region of cortical and trabecular bone each were scanned as comparison for each material (two cortical regions for titanium). Due to delays in sample processing, no samples of PEEK at the 4 week time point were processed for SAXS and XRD measurements.

2.5. Data processing

Data processing prior to and including azimuthal integration was performed using DAWN Science (Diamond Light Source) [29]. In particular, dead pixels were removed from the SAXS data using a geometric mask, the q-range was calibrated using the obtained calibration data. In the case of the XRD data hot pixels were removed using a threshold set to an intensity of 1000 a.u. and the q-range was calibrated with the respective calibration data. Both data sets were then integrated azimuthally and stored into text files for further processing with Matlab R2017b (The MathWorks Inc., USA). The platelet thickness was computed from the SAXS data using the stack of cards model [30]. The HAP orientation can be computed from the SAXS signal as HAP c-axis and collagen fibers are aligned in parallel, thus resulting in an anisotropic SAXS signal. Therefore, a sine wave was fitted to the SAXS signal initially and refined using a Gaussian curve to estimate the exact position and the area of the peak. The degree of orientation was computed by the ratio of the integrated signal intensity of the Gaussian sum of the total area incl. the background [31]. This factor thus gives the fraction of the oriented material and ranges between 0 (no preferential orientation) and 1 (fully ordered), i.e. a value of 0.2 indicates that 20% of the material in the probed area is oriented in the same direction. The lattice constant for the (310) reflex of hydroxyapatite was computed from the XRD data via the peak position of a Gaussian fit and the crystal width was computed using the Scherrer equation [32]. We decided to focus on the (310) reflection as this was strongest one in our detectable XRD range as the setup was optimized for SAXS. See Fig. 2 for a schematic of the computed parameters.

For the subsequent analysis, the scanned regions were identified within the thin section mounted on kapton tape using light microscopy. Using Avizo 9.4 (FEI SAS, Thermo Scientific™, France) the regions were segmented into bone, degradation layer and background via visual comparison with the optical image. Fig. 3 shows the segmented image for the scanned region depicted in Fig. 1. The average of each computed parameter was then determined for the pixels identified as bone for each region. For comparison, mean lattice spacing and crystal width were also determined for the region area defined as degradation layer. The divergence of the orientation for each scanned region was computed using Matlab to assess the similarity of orientations between different pixels within this region. The lower the divergence, the more similar the orientations. The gradient function in Matlab was used to determine the surface orientation of the bone. It was then compared to the HAP orientation using Matlab. Subsequently, Matlab was also used to perform the final analysis (means and standard deviations) of all determined parameters.

3. Statistical methods

From each scanned region, the mean of each computed parameter was determined. For the regions of the corresponding material and time point, the overall mean value and standard deviation of these means were then computed. These are displayed in the graphs to follow. A one-way analysis of variance (ANOVA) with a Bonferroni correction was conducted to determine statistically significant differences between the parameters at the bone-implant interface for the different implant materials overall (p_{all}) and for

each healing time (p_4, p_8, p_{12}). I.e., for p_4 the values for a parameter of the 4 week interface regions were compared, whereas for p_{all} the values of all time points of the interface regions were taken into account. Additionally, for each material, the computed parameters at each time point were compared against each other and against trabecular and cortical regions, respectively. The corresponding p-values are denoted e.g., by $p_{Ti-4,8}$ when the 4 and 8 week time points in titanium are compared, or $p_{5Gd-12, trab}$ when 12 week time point and trabecular region of bone surrounding Mg-5Gd implants are compared. For legibility, any determined significance was not highlighted in figures but only within the text.

4. Results

Fig. 4 shows maps of the different computed parameters, i.e., HAP orientation and degree of orientation (Fig. 4(a)), HAP platelet thickness (Fig. 4(b)), (310) lattice spacing (Fig. 4(c)) and crystallite size (Fig. 4(d)) for the exemplary region highlighted in Fig. 1.

Differences in the parameters can be seen between the upper left corner, in which a part of the implant degradation layer is visible and the right hand side of the region, which contains bone. Furthermore, the bone appears inhomogeneous, in particular with respect to orientation. The fit of the stack of cards model designed to determine the platelet thickness becomes untrustworthy within the degradation layer and near the implant interface and has therefore been excluded from the figure and the analysis in these instances.

In the following, we are presenting the quantitative evaluation of all 57 scanned interface regions and 8 trabecular and cortical references.

4.1. Hydroxyapatite platelet orientation

Fig. 5(a) shows the degree of orientation in the bone surrounding titanium, PEEK, Mg-5Gd and Mg-10Gd implants for 4, 8 and 12 weeks healing times and in reference regions in trabecular and cortical bone averaged over the respective regions. To determine how similarly the platelets were aligned, the mean divergence of the orientation map was computed for each region, see Fig. 5(b). Furthermore, the difference between bone interface orientation and HAP orientation at the interface was computed (Fig. 5(c)). There is no significant difference in degree of orientation between the materials and healing times. However, there is a trend showing that the degree of orientation in bone surrounding titanium implants is higher (0.11–0.19) than that around PEEK (0.05–0.13), Mg-5Gd (0.04–0.07) and Mg-10Gd implants (0.04–0.13). The divergence of orientation is significantly different over all time points only between titanium and Mg-5Gd ($p_{all} < 0.001$). The general magnitude of the divergence between 0.1 and 0.4 suggests a fairly well ordered orientation map. However, a difference of 15°–50° was found when comparing the bone surface orientation at the implant interface to the HAP orientation at the interface, thus indicating no preferential orientation of the HAP at the implant surface. No significant differences were found for the evolution of degree of orientation, divergence of orientation or difference in surface to HAP orientation over time or between the trabecular and cortical regions and interface regions.

4.2. Hydroxyapatite platelet thickness

The HAP platelet thickness was computed from the SAXS signal and is displayed in Fig. 6. Overall, the mean platelet thicknesses for each material and time point are in ranges between 23–46 Å. There were however no statistically significant differences between materials, except between PEEK and Mg-10Gd at the 8 week time point (PEEK vs. Mg-10Gd $p_8 < 0.05$). Furthermore, no significant

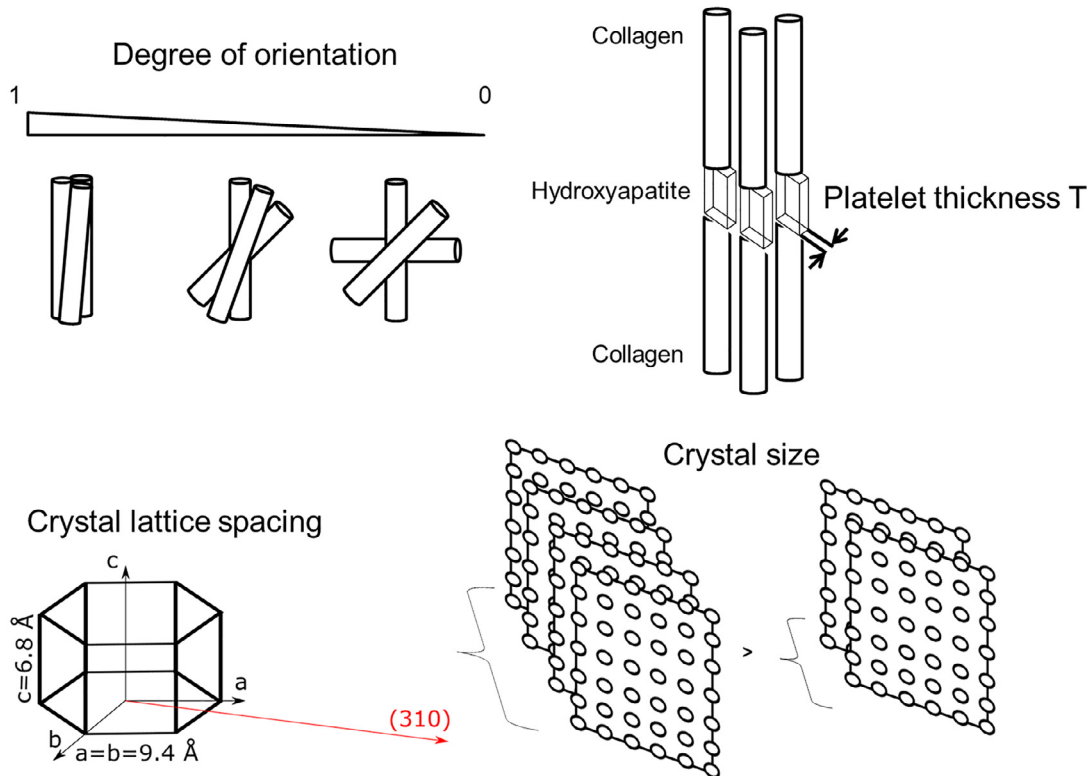


Fig. 2. Explanatory schematic of the computed parameters. The degree of orientation and thickness of the hydroxyapatite platelets are shown as well as the crystal lattice spacing and crystal size.

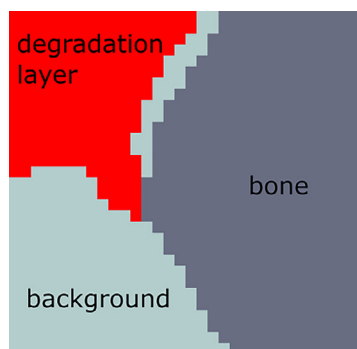


Fig. 3. Segmentation example of scanned region displayed in Fig. 1 (Mg-5Gd implant with 12 week healing time).

differences were found for the evolution of platelet thickness over time or between the trabecular and cortical regions and interface regions.

4.3. Lattice spacing

The lattice spacing for the (310) reflection of the HAP in bone was computed from the XRD data, see Fig. 7(a). Similarly, the spacing was computed within the degradation layer of the Mg-5Gd and Mg-10Gd implant and compared to the bone signal, as shown in Fig. 7(b). The computed lattice spacing of the (310) reflection is significantly higher around a titanium implant than for Mg-xGd implants (Ti vs. Mg-10Gd $p_{\text{all}} < 0.001$, Ti vs. Mg-5Gd $p_{\text{all}} < 0.05$). The (310) reflection in bone surrounding PEEK implants, however, differs neither significantly from bone surrounding Mg-xGd nor titanium implants (Ti vs. PEEK $p_{\text{all}} = 0.087$). The lattice spacing

within the degradation layer as displayed in Fig. 7b further differs significantly from that in bone for Mg-10Gd ($p_{\text{all}} < 0.001$). No significant differences were found for the evolution of lattice spacing over time or between the trabecular and cortical regions and interface regions in the same material.

4.4. Crystal size

The crystal size was computed from the XRD signal of the (310) reflection and is shown in Fig. 8(a) for different implant materials and healing times. Fig. 8(b) shows the difference in crystallite size between bone and degradation layer for Mg-5Gd and Mg-10Gd. A significant difference is apparent between Mg-5Gd and titanium surrounding bone ($p_{\text{all}} < 0.01$, $p_{12} < 0.05$), as well as between bone and degradation layer for Mg-10Gd ($p_{\text{all}} < 0.001$). Whilst no significant differences were found for the temporal evolution of crystal size, bone surrounding PEEK showed a significant difference in crystal size between 8 and 12 week time points and the scanned cortical region ($p_{\text{Pe-8,cort}} < 0.05$, $p_{\text{Pe-12,cort}} < 0.05$).

5. Discussion

5.1. Hydroxyapatite platelet orientation

The mean degree of orientation of bone surrounding titanium implants in this study is generally lower than that found previously for bone forming around intramedullary nails (0.22–0.25) [23]. Bone surrounding Mg-based alloys was found to be in a similar range, though slightly lower in newly formed bone in the implant region after 15 months healing time [22]. However, previous results lacked statistical power and the results shown in this study show a large deviation even among the same material. Overall, it

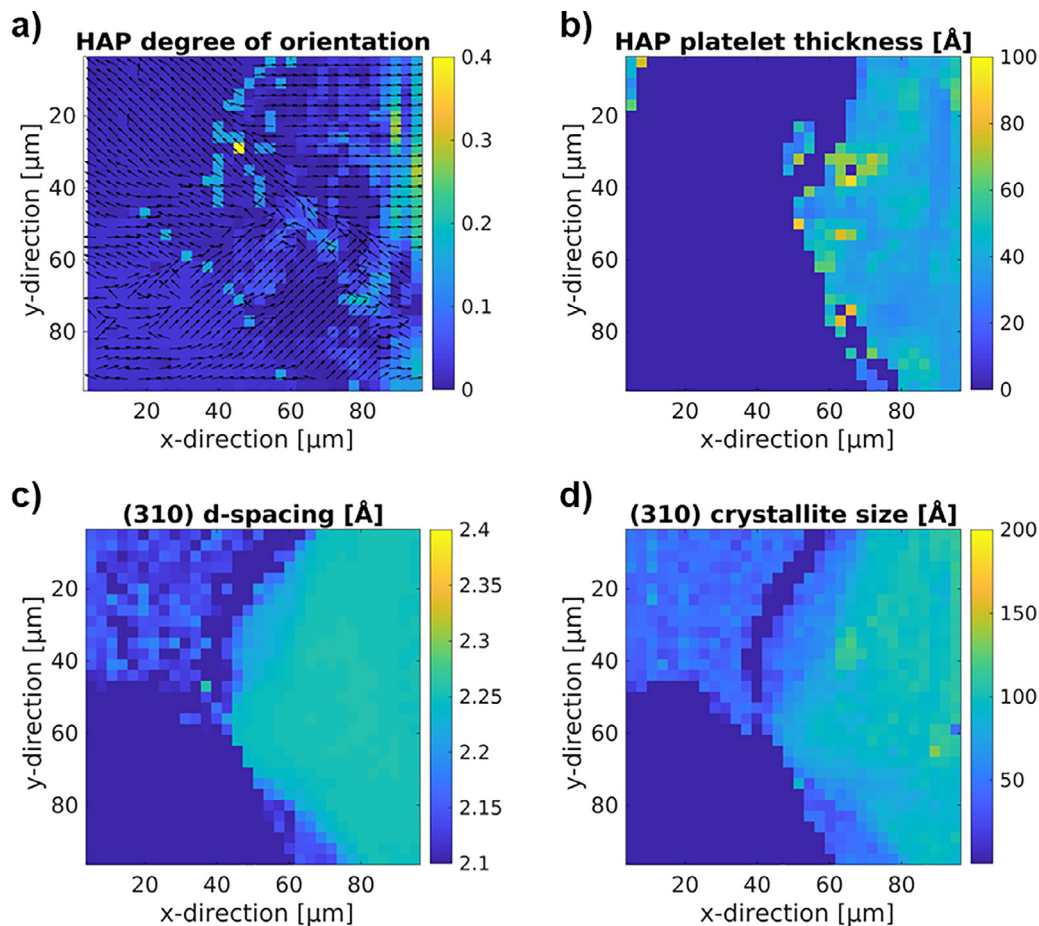


Fig. 4. Computed ultrastructural parameters for exemplary region from Fig. 1 (Mg-5Gd implant with 12 week healing time). (a) HAP platelet orientation (arrows) and degree of orientation (color scale), (b) HAP platelet thickness, (c) (310) lattice spacing and d) (310) crystallite size.

appears that the mineralization of HAP around titanium implants takes place in a more oriented way as the degree of orientation is higher and divergence lower. The standard deviations are however very large such that no statistical significance can be derived.

5.2. Hydroxyapatite platelet thickness

The computed mean platelet thicknesses for titanium of 32–36 Å are higher than those found in the literature, which ranged between 20 and 25 Å [23,24], this may be due to a use of different animals, implantation sites and healing times (intramedullary nail in rats after 8 weeks [23] and intervertebral disk space in pigs after 6 months [24]). On the other hand, the average thickness com-

puted for Mg-5Gd (27–36 Å) and Mg-10Gd (25–32 Å) is similarly higher than that reported for other Mg-based alloys (19–23 Å) [22], which therefore shows a systemic but comparable difference.

5.3. Lattice spacing

The computed lattice spacing for the bone surrounding degradable implants and PEEK (2.257–2.263 Å for Mg-10Gd, 2.263–2.272 Å for Mg-5Gd, 2.264–2.275 Å for PEEK) is closer to that recorded for HAP (2.26–2.27 Å) [16,33,34], than the lattice spacing measured in bone surrounding titanium implants (2.281–2.292 Å). A comparison of the (310) signal between bone at the implant

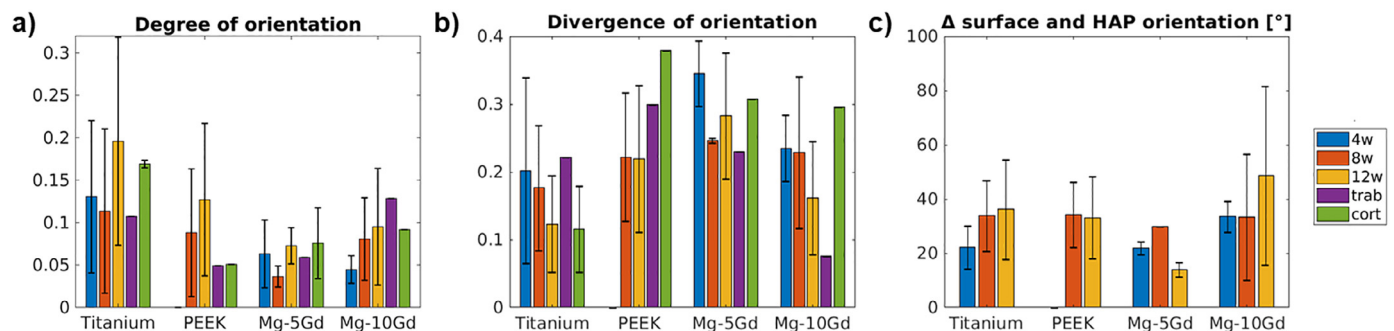


Fig. 5. (a) Degree of orientation, (b) divergence of orientation and (c) difference in surface and hydroxyapatite orientation at the surface surrounding titanium, PEEK, Mg-5Gd and Mg-10Gd implants for 4, 8 and 12 weeks healing times and reference regions in trabecular and cortical bone. Results are shown as mean \pm standard deviation.

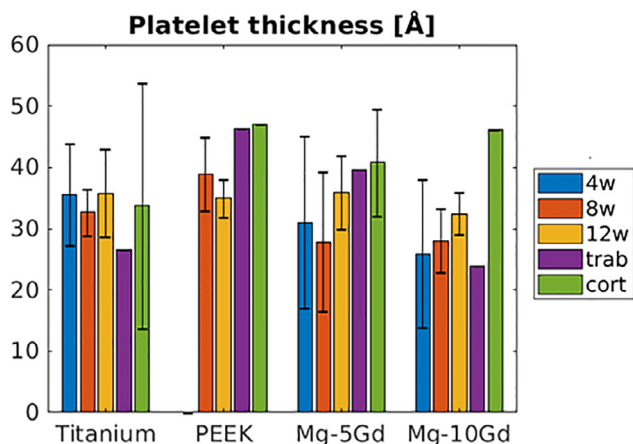


Fig. 6. Hydroxyapatite platelet thickness in bone surrounding titanium, PEEK, Mg-5Gd and Mg-10Gd implants for 4, 8 and 12 weeks healing times and reference regions in trabecular and cortical bone. Results are shown as mean \pm standard deviation.

interface and regions of degradation layer of Mg-xGd shows a significant shift to a smaller lattice spacing in the degraded implant, see also Figs. 1 and 3, which may be indicative of the formed apatite including significant amounts of magnesium or gadolinium instead of calcium within the degradation layer, in contrast to the surrounding bone [21,35]. We note that the incorporation of Mg or Gd is only deduced by the shift of the diffraction peak position. As these changes are more pronounced in regions characterized as degradation layer, this is the most reasonable explanation which has also been observed by other authors [21]. This is in agreement with previous in vivo studies that have shown that whilst the degradation layer of Mg alloys does contain calcium and phosphorus, Mg is also still visible within [9]. The difference in lattice spacing between titanium, PEEK and Mg-xGd implants may be a result of the different mechanical properties, in particular the Young's modulus, of the different implant materials. The Young's modulus of Mg-xGd alloys and PEEK (approx. 45 GPa [36] and 4 GPa [37], respectively) is more similar to that of bone [21,22] and much lower than that of titanium (105–118 GPa [38]), thus presumably resulting in a different fluid flow and thus mechanical stimulus experienced by the surrounding osteocytes, which in turn influences the mineralization of the new bone.

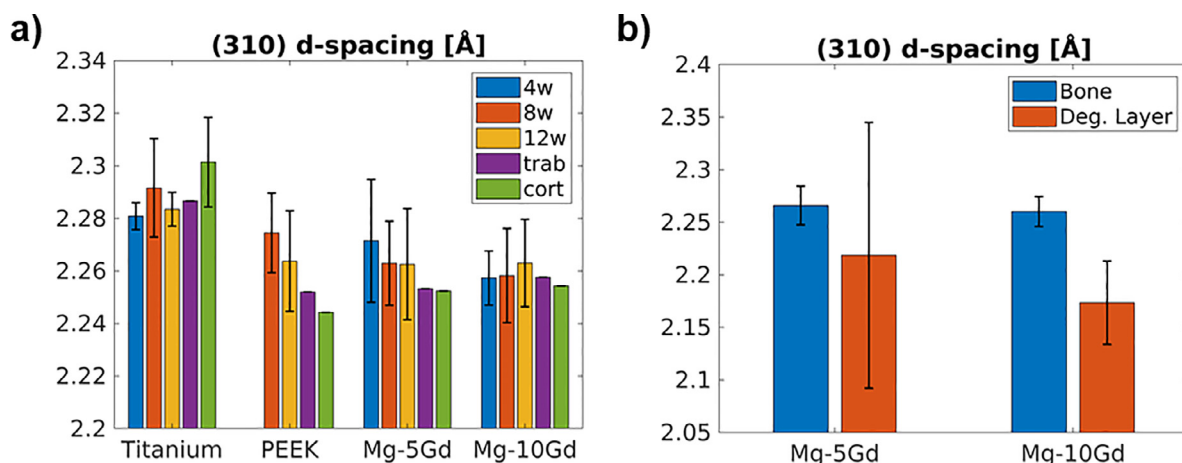


Fig. 7. Lattice spacing of the (a) (310) hydroxyapatite reflection in bone surrounding titanium, PEEK, Mg-5Gd and Mg-10Gd implants for 4, 8 and 12 weeks healing times and reference regions in trabecular and cortical bone. (b) Comparison of the mean lattice spacing over all time points within implant degradation layer and bone of the (310) reflection. Results are shown as mean \pm standard deviation.

5.4. Crystal size

The crystal size of Mg-10Gd is in a similar range to that previously found for other biodegradable Mg alloys [21]. Changes in the (310) crystal size of the HAP have been shown to correlate with a deposit of Mg in the bone matrix, i.e. where normal levels of Mg are found the crystal size ranges between 55 and 70 Å and in regions where an increase of Mg was seen the crystal size dropped to 40–50 Å [21]. Similarly, the crystal size has been shown to decrease with increasing levels of Mg in synthesized Mg substituted HAP [39,40]. Whilst the crystallite size of Mg-5Gd and Ti are significantly different, there is no such difference in comparison to PEEK, thus not yielding conclusive evidence that Mg or Gd are deposited within the bone matrix. However, the HAP-like crystal structure of the degradation layer of Mg-xGd screws is displaying a shift to lower (310) crystallite sizes and more so for a higher Gd content, which is thought to be indicative of incorporation of Gd into the corrosion product.

6. Conclusion

In the first study presenting a quantitative comparison of the bone ultrastructure around biodegradable Mg-based alloys and PEEK and titanium implants, we have shown that most of the ultrastructural parameters, in particular the degree of orientation and other orientation parameters, as well as the hydroxyapatite platelet thickness, don't differ significantly between materials. The (310) lattice spacing and crystal size however are impacted and differ significantly between bone surrounding titanium and Mg-based alloys. This may indicate the possible deposition of Mg within the bone matrix. Furthermore, analysis of the degradation layer of Mg-xGd implants shows that whilst apatite formation can be observed, its lattice spacing and crystal size differ significantly from that in the surrounding bone. This may be due to the incorporation of Gd into the apatite, which requires further investigation of the elemental composition of the different regions. This is particularly relevant, as Gd remains controversial in terms of its unknown health impact [41,42], and a local deposition of Gd at the implant site may be beneficial.

To determine whether the presented two-dimensional investigation of the ultrastructure is missing information, future studies may employ three-dimensional techniques of imaging the ultrastructure [43–45]. Additionally, methods determining element composition need to be employed to support the hypothesis on Mg and Gd incorporation resulting from this study. Furthermore, the

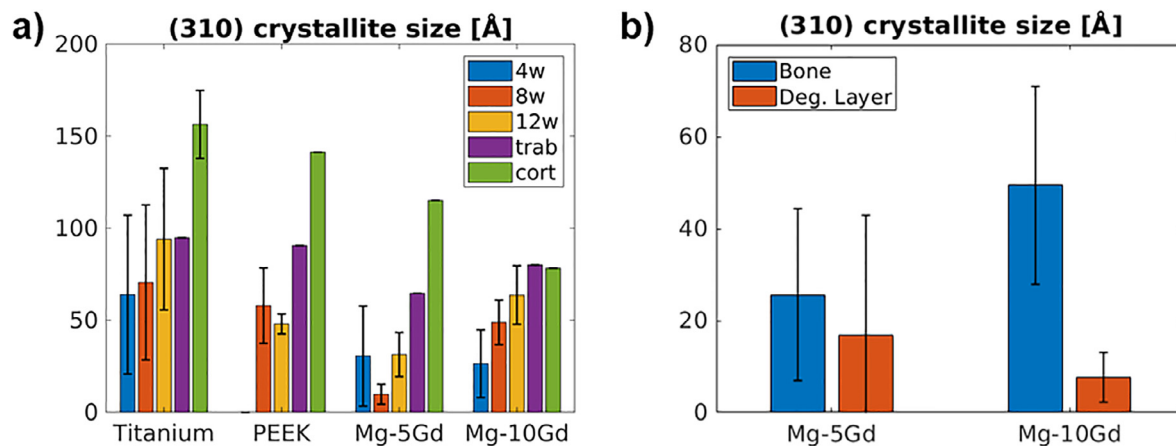


Fig. 8. (a) (310) crystallite size in bone surrounding titanium, PEEK, Mg-5Gd and Mg-10Gd implants for 4, 8 and 12 weeks healing times and reference regions in trabecular and cortical bone. (b) Difference in (310) crystallite size for bone and degradation layer around Mg-5Gd and Mg-10Gd implants. Results are shown as mean \pm standard deviation.

influence of the implant mechanical properties on the bone should be investigated in more detail and compared to osseointegration indicators on the micro- to millimeter scale (e.g., bone-to-implant contact).

Declaration of Competing Interest

The authors declare that they have no known competing financial interests or personal relationships that could have appeared to influence the work reported in this paper.

CRediT authorship contribution statement

Berit Zeller-Plumhoff: Conceptualization, Project administration, Formal analysis, Writing - review & editing. **Carina Malich:** Formal analysis. **Diana Krüger:** Project administration. **Graeme Campbell:** Project administration. **Björn Wiese:** Resources. **Silvia Galli:** Resources. **Ann Wennerberg:** Conceptualization. **Regine Willumeit-Römer:** Conceptualization. **D.C. Florian Wieland:** Formal analysis, Conceptualization, Project administration.

Funding sources

Funding was provided by the Röntgen-Ångström Cluster in project SynchroLoad (05K16CGA), Swedish Research Council 2015-06109, and by the German Bundesministerium für Bildung und Forschung in project MgBone (05K16CGB).

Acknowledgment

The authors thank Anton Davydok for support at the beamline, Heiko Richter from LLS Rowiak Laser Lab Solutions for processing of samples for X-ray analysis and Thomas Dose for construction of the sample holder frame. We also thank DESY for granting P03 beamtimes 11003686 and 11005218.

Supplementary materials

Supplementary material associated with this article can be found, in the online version, at doi:[10.1016/j.actbio.2019.11.030](https://doi.org/10.1016/j.actbio.2019.11.030).

References

- [1] F. Witte, N. Hort, C. Vogt, S. Cohen, K. Kainer, R. Willumeit, F. Feyerabend, Degradable biomaterials based on magnesium corrosion, *Curr. Opin. Solid State Mater. Sci.* 12 (5–6) (2008) 63–72.
- [2] F. Feyerabend, J. Fischer, J. Holtz, F. Witte, R. Willumeit, H. Drucker, C. Vogt, N. Hort, Evaluation of short-term effects of rare earth and other elements

- used in magnesium alloys on primary cells and cell lines, *Acta Biomater.* 6 (5) (2010) 1834–1842.
- [3] N. Hort, Y. Huang, D. Fehner, M. Stormer, C. Blawert, F. Witte, C. Vogt, H. Drucker, R. Willumeit, K. Kainer, F. Feyerabend, Magnesium alloys as implant materials - Principles of property design for Mg-Re alloys, *Acta Biomater.* 6 (5) (2010) 1714–1725.
- [4] A. Sanchez, B. Luthringer, F. Feyerabend, R. Willumeit, Mg and Mg alloys: how comparable are in vitro and in vivo corrosion rates? A review, *Acta Biomater.* 13 (2015) 16–31.
- [5] F. Cecchinato, N. Agha, A. Martinez-Sanchez, B. Luthringer, F. Feyerabend, R. Jimbo, R. Willumeit-Romer, A. Wennerberg, Influence of magnesium alloy degradation on undifferentiated human cells, *PLoS ONE* 10 (11) (2015) 1–18.
- [6] N. Agha, F. Feyerabend, B. Mihailova, S. Heidrich, U. Bismayer, R. Willumeit-Romer, Magnesium degradation influenced by buffering salts in concentrations typical of in vitro and in vivo models, *Mater. Sci. Eng. C Mater. Biol. Appl.* 58 (2016) 817–825.
- [7] N. Agha, R. Willumeit-Romer, D. Laipple, B. Luthringer, F. Feyerabend, The degradation interface of magnesium based alloys in direct contact with human primary osteoblast cells, *PLoS ONE* 11 (6) (2016) 1–20.
- [8] A. Myrissa, N. Agha, Y. Lu, E. Martinelli, J. Eichler, G. Szakacs, C. Kleinhans, R. Willumeit-Romer, U. Schafer, A. Weinberg, In vitro and in vivo comparison of binary mg alloys and pure Mg, *Mater. Sci. Eng. C Mater. Biol. Appl.* 61 (2016) 865–874.
- [9] I. Marco, A.A. Myrissa, E. Martinelli, F. Feyerabend, R. Willumeit-Römer, A. Weinberg, O. Van der Biest, In vivo and in vitro degradation comparison of pure Mg, Mg-10Gd and Mg-2Ag: a short term study, *eCells Mater. J.* (2017) 90–104.
- [10] S. Weiner, H.D. Wagner, THE material BONE: structure-Mechanical function relations, *Ann. Rev. Mater. Sci.* 28 (1) (1998) 271–298.
- [11] D.S. Bocciarelli, Morphology of crystallites in bone, *Calcif. Tissue Res.* 5 (3) (1970) 261–269.
- [12] E. Beniash, Biominerals-hierarchical nanocomposites: the example of bone, *Wiley Interdiscip. Rev. Nanomed. Nanobiotechnol.* 3 (1) (2011) 47–69.
- [13] R.A. Robinson, An electron-microscopic study of the crystalline inorganic component of bone and its relationship to the organic matrix, *J. Bone Joint Surg. Am.* 34-A (2) (1952) 389–435 passim.
- [14] S. Weiner, W. Traub, Bone structure: from angstroms to microns, *FASEB J* 6 (3) (1992) 879–885.
- [15] P. Fratzl, S. Schreiber, K. Klaushofer, Bone mineralization as studied by small-angle X-Ray scattering, *Connect. Tissue Res.* 34 (4) (1996) 247–254.
- [16] A.S. Posner, A. Perloff, A.F. Diorio, Refinement of the hydroxyapatite structure, *Acta Crystallogr.* 11 (4) (1958) 308–309.
- [17] S. Rinnerthaler, P. Roschger, H.F. Jakob, A. Nader, K. Klaushofer, P. Fratzl, Scanning small angle X-ray scattering analysis of human bone sections, *Calcif. Tissue Int.* 64 (5) (1999) 422–429.
- [18] T. Nakano, K. Kaibara, Y. Tabata, N. Nagata, S. Enomoto, E. Marukawa, Y. Umakoshi, Unique alignment and texture of biological apatite crystallites in typical calcified tissues analyzed by microbeam X-ray diffractometer system, *Bone* 31 (4) (2002) 479–487.
- [19] M. Georgiadis, R. Muller, P. Schneider, Techniques to assess bone ultrastructure organization: orientation and arrangement of mineralized collagen fibrils, *J. R. Soc. Interface* 13 (119) (2016).
- [20] N.P. Camacho, L. Hou, T.R. Toledano, W.A. Ilg, C.F. Brayton, C.L. Raggio, L. Root, A.L. Boskey, The material basis for reduced mechanical properties in oim mice bones, *J. Bone Miner Res.* 14 (2) (1999) 264–272.
- [21] T. Grunewald, H. Rennhofer, B. Hesse, M. Burghammer, S. Stanzl-Tschegg, M. Cotte, J. Löffler, A. Weinberg, H. Lichtenegger, Magnesium from biore-sorbable implants: distribution and impact on the nano- and mineral structure of bone, *Biomaterials* 76 (2016) 250–260.

- [22] T.A. Grünewald, A. Ogier, J. Akbarzadeh, M. Meischel, H. Peterlik, S. Stanzl-Tschegg, J.F. Löffler, A.M. Weinberg, H.C. Lichtenegger, Reaction of bone nanostructure to a biodegrading magnesium WZ21 implant – a scanning small-angle X-ray scattering time study, *Acta Biomater.* 31 (2016) 448–457.
- [23] R.M. Hoerth, M.R. Katunar, A. Gomez Sanchez, J.C. Orellano, S.M. Ceré, W. Wagermaier, J. Ballarre, A comparative study of zirconium and titanium implants in rat: osseointegration and bone material quality, *J. Mater. Sci. Mater. Med.* 25 (2) (2014) 411–422.
- [24] M.H. Bünger, M. Foss, K. Erlacher, H. Li, X. Zou, B.L. Langdahl, C. Bünger, H. Birkedal, F. Besenbacher, J.S. Pedersen, Bone nanostructure near titanium and porous tantalum implants studied by scanning small angle x-ray scattering, *Eur. Cell Mater.* 12 (2006) 81–91.
- [25] S. Galli, On Magnesium-containing Implants for Bone Applications, Faculty of Odontology, Malmö University, 2016.
- [26] J. Moosmann, B. Zeller-Plumhoff, D.C.F. Wieland, S. Galli, D. Krüger, T. Dose, H. Burmester, F. Wilde, M. Bech, N. Peruzzi, B. Wiese, A. Hipp, F. Beckmann, J. Hammel, R.W. Illumeit-Römer, Biodegradable magnesium-based implants in bone studied by synchrotron radiation microtomography, in: *Proceedings of the SPIE 10391, Developments in X-Ray Tomography XI, 1039100*, 2017.
- [27] A. Buffet, A. Rothkirch, R. Döhrmann, V. Körstgens, M.M. Abul Kashem, J. Perlich, G. Herzog, M. Schwartzkopf, R. Gehrke, P. Müller-Buschbaum, S.V. Roth, P03, the microfocus and nanofocus X-ray scattering (MiNaXS) beamline of the Petra III storage ring: the microfocus endstation, *J. Synchrotron. Radiat.* 19 (Pt 4) (2012) 647–653.
- [28] C. Krywka, H. Neubauer, M. Priebe, T. Salditt, J. Keckes, A. Buffet, S.V. Roth, R. Doehrmann, M. Mueller, A two-dimensional waveguide beam for X-ray nanodiffraction, *J. Appl. Crystallogr.* 45 (1) (2012) 85–92.
- [29] J. Filik, A.W. Ashton, P.C.Y. Chang, P.A. Chater, S.J. Day, M. Drakopoulos, M.W. Gerring, M.L. Hart, O.V. Magdysyuk, S. Michalik, A. Smith, C.C. Tang, N.J. Terrill, M.T. Wharmby, H. Wilhelm, Processing two-dimensional X-ray diffraction and small-angle scattering data in, *J. Appl. Crystallogr.* 50 (Pt 3) (2017) 959–966.
- [30] A. Gourrier, C. Li, S. Siegel, O. Paris, P. Roschger, K. Klaushofer, P. Fratzl, Scanning small-angle X-ray scattering analysis of the size and organization of the mineral nanoparticles in fluorotic bone using a stack of cards model, *J. Appl. Crystallogr.* 43 (6) (2010) 1385–1392.
- [31] S. Pabisch, W. Wagermaier, T. Zander, C. Li, P. Fratzl, Imaging the nanostructure of bone and dentin through small- and wide-angle X-ray scattering, *Methods Enzymol.* 532 (2013) 391–413.
- [32] P. Scherrer, Bestimmung der gröÙe und der inneren struktur von kolloidteilchen mittels röntgenstrahlen, *nachrichten von der gesellschaft der wissenschaften, göttingen, Math. Phys. Klasse 2* (1918) 98–100.
- [33] R.M. Wilson, J.C. Elliott, S.E.P. Dowker, Rietveld refinement of the crystallographic structure of human dental enamel apatites, *Am. Mineralog.* (1999) 1406.
- [34] J.M. Hughes, M. Cameron, K.D. Crowley, Structural variations in natural F, OH, and Cl apatites, *Am. Mineralog.* 74 (7–8) (1989) 870–876.
- [35] Y. Li, C.P. Ooi, C. Philip Hong Ning, K. Aik Khor, Synthesis and characterization of neodymium(iii) and gadolinium(iii)-substituted hydroxyapatite as biomaterials, *Int. J. Appl. Ceram. Technol.* 6 (4) (2009) 501–512.
- [36] Y. Xu, J. Li, Z. Zhong, K. Kainer, N. Hort, Effects of Gadolinium and Neodymium Addition on Young's Modulus of Magnesium-Based Binary Alloys, *Magnesium Technology 2017*, Springer International Publishing, 2017.
- [37] J. Sandler, P. Werner, M.S.P. Shaffer, V. Demchuk, V. Altstädt, A.H. Windle, Carbon-nanofibre-reinforced poly(ether ether ketone) composites, *Compos. Part A Appl. Sci. Manufact.* 33 (8) (2002) 1033–1039.
- [38] W.D. Callister, *Materials Science and Engineering: An Introduction*, John Wiley & Sons, Inc, New York, 2007.
- [39] E. Bertoni, A. Bigi, G. Cojazzi, M. Gandolfi, S. Panzavolta, N. Roveri, Nanocrystals of magnesium and fluoride substituted hydroxyapatite, *J. Inorg. Biochem.* 72 (1–2) (1998) 29–35.
- [40] A. Bigi, G. Falini, E. Foresti, A. Ripamonti, M. Gazzano, N. Roveri, Magnesium influence on hydroxyapatite crystallization, *J. Inorg. Biochem.* 49 (1) (1993) 69–78.
- [41] A. Myrissa, S. Braeuer, E. Martinelli, R. Willumeit-Römer, W. Goessler, A.M. Weinberg, Gadolinium accumulation in organs of Sprague-Dawley® rats after implantation of a biodegradable magnesium-gadolinium alloy, *Acta Biomater.* 48 (2017) 521–529.
- [42] J. Ramalho, R.C. Semelka, M. Ramalho, R.H. Nunes, M. AlObaidy, M. Castillo, Gadolinium-based contrast agent accumulation and toxicity: an update, *AJNR Am. J. Neuroradiol.* 37 (7) (2016) 1192–1198.
- [43] M. Georgiadis, Guizar-Sicarios M., Zwahlen A., Trüssel A.J., Bunk O., Müller R., Schneider P., 3D scanning SAXS: a novel method for the assessment of bone ultrastructure orientation, 71 (2015) 42–52.
- [44] M. Liebi, M. Georgiadis, A. Menzel, P. Schneider, J. Kohlbrecher, O. Bunk, M. Guizar-Sicarios, Nanostructure surveys of macroscopic specimens by small-angle scattering tensor tomography, *Nature* 527 (7578) (2015) 349.
- [45] F. Schaff, M. Bech, P. Zaslansky, C. Jud, M. Liebi, M. Guizar-Sicarios, F. Pfeiffer, Six-dimensional real and reciprocal space small-angle X-ray scattering tomography, *Nature* 527 (7578) (2015) 353.